


Article

Fe Single Atoms Reduced by NaBH_4 Mediate $\text{g-C}_3\text{N}_4$ Electron Transfer and Effectively Remove 2-Mercaptobenzothiazole

Chen Yang, Xuefeng Hu *, Yaxing Bai, Beichuan Cai and Yujie Li

School of Environmental Science and Engineering, Shaanxi University of Science and Technology, Xi'an 710021, China

* Correspondence: huxuefeng@sust.edu.cn

Abstract: In this study, a simple and low-energy synthesis scheme of Fe single-atom anchored carbon nitride was reported to improve the photocatalytic performance of $\text{g-C}_3\text{N}_4$. Synthesized Fe single-atom doped graphite carbon nitride (Fe-SACs/ $\text{g-C}_3\text{N}_4$) showed high activity and stability for the degradation of 2-mercaptobenzothiazole (MBT); under visible light irradiation, 99% of MBT could be degraded within 35 min, and the degradation ability basically did not decline after five cycles, mainly due to the synergistic effect of the Fe single atoms and carbon nitride. The results of X-ray absorption fine structure (EXAFS), X-ray photoelectron spectroscopy (XPS), and density functional theory calculations show that the single-atom Fe forms Fe-N₄ coordination with pyridine nitrogen to generate a new electron transfer channel, which can significantly improve the in-plane separation and transfer of carriers, finally enhancing the generation of superoxide radicals. This is confirmed by time-resolved photoluminescence, photoelectron chemistry, and electron spin resonance measurements. The main intermediates of MBT degradation were determined using a liquid chromatograph–mass spectrometer (LC-MS), and a possible photocatalytic mechanism based on the quenching experiment and electron paramagnetic resonance (EPR) test was proposed. A deep understanding of the contribution of Fe single-atom sites with clear local coordination structures will help to design effective catalysts for photocatalytic performance.

Keywords: graphitic carbon nitride; single-atom; NaBH_4 reduction; photocatalytic degradation

Citation: Yang, C.; Hu, X.; Bai, Y.; Cai, B.; Li, Y. Fe Single Atoms Reduced by NaBH_4 Mediate $\text{g-C}_3\text{N}_4$ Electron Transfer and Effectively Remove 2-Mercaptobenzothiazole. *Catalysts* **2023**, *13*, 619. <https://doi.org/10.3390/catal13030619>

Academic Editor: Da-Ren Hang

Received: 28 February 2023

Revised: 14 March 2023

Accepted: 17 March 2023

Published: 20 March 2023



Copyright: © 2023 by the authors. Licensee MDPI, Basel, Switzerland. This article is an open access article distributed under the terms and conditions of the Creative Commons Attribution (CC BY) license (<https://creativecommons.org/licenses/by/4.0/>).

1. Introduction

As global industrialization accelerates and the world's population grows [1–3], a large number of organic substances, such as antibiotics, organic dyes, and pesticides, are released into different kinds of water every day [4–6]. It is important to adopt efficient methods to eliminate these organic pollutants from the environment. 2-Mercaptobenzothiazole (MBT) is an organic substance widely used in medicine, rubber vulcanization accelerators, antidotes, synthetic fungicide raw materials, and other fields [7]. In recent years, it has often been found in wastewater treatment plants and in anaerobic sludge digestion, where it is not easily degraded by biological treatment [8]. Therefore, removing MBT from wastewater is of great significance for ecological development and human health. As a semiconductor photocatalyst [9–12], $\text{g-C}_3\text{N}_4$ has attracted extensive attention because of its light stability, nontoxicity, and appropriate water treatment potential. However, the poor electron transfer ability, low specific surface area and low absorption efficiency of visible light exhibited by bulk $\text{g-C}_3\text{N}_4$ limit its development [13,14]. Various modification strategies reported in the literature have been able to achieve better photocatalytic performance, among which metal doping is considered to be one of the most effective methods [15–18]. The activity of iron-doped carbon nitride has improved, but it is still unsatisfactory [19,20].

Transition metal single-atom catalysts (SACs) have received much attention in the field of heterogeneous catalysis due to their high metal utilization, low cost, and favorable catalytic activity. However, in many cases, single-atom catalysts are not sufficiently stable.

As we all know, the surface free energy of metals increases as the particle size of the metal decreases, which leads to the clustering of isolated individual atoms into nanoparticles during the synthesis and reaction. This is a significant challenge for the stability of SACs. To overcome this problem [21], the construction of strong covalent coordination interactions between the central metal single atom and the surrounding ligand atoms is essential [22,23]. The typical two-dimensional (2D) layered structure of g-C₃N₄ brings abundant surface loading sites. Adjacent layers are connected by weak van der Waals forces, and in-plane C and N atoms hybridize with sp² to form a highly exotic π -conjugated system [24]. The existence of a lone pair of electrons in the N atom provides an opportunity for the coordination of metal atoms. The abundant lone pair electrons of N atoms in CN heterocycles can confine highly reactive single metal atoms, thereby producing a stable g-C₃N₄-based single-atom photocatalyst. Therefore, g-C₃N₄ is an ideal carrier material for loading single atoms [25–28].

Generally, the methods for synthesizing single-atom catalysts include direct synthesis and post-synthesis [29]. The direct synthesis method usually involves high-temperature calcination in an inert atmosphere, and the synthesis is carried out with or without a template. Guo and co-workers [30] used C₃N₄ to synthesize FeN_x/C₃N₄ using the template pyrolysis method, and synthesized iron precursor (Fe-ICC) synthesis using ball milling, followed by the complete grinding of the purified iron precursor and melamine in an agate mortar. Finally, the whole mixture was calcined at 600 °C for 5 h under inert conditions. However, the preparation process for the hard template method is complicated, the cost is high, the metal leaching activity is high, and the stripping process is complicated and necessary. Especially with the heated acid treatment, the choice of different leaching solutions can have a significant effect on the active metal [31]. Wang and co-workers [32] used a template-free strategy to synthesize a two-dimensional Fe/N co-doped carbon network (C₃N₄) as an efficient catalyst for ORR. In their work, melamine and chlorinated 1,10-phenanthroline were dispersed and polymerized under argon at 600 or 800 °C for 2 h. The subsequent black powder was treated with 1 M sulfuric acid and pyrolyzed again at 800 °C for 1 h, resulting in the final Fe-NC-PT catalyst. This kind of synthesis method will produce high energy consumption and is still hampered by low metal loading. The post-synthesis method refers to the loading of metal ions on carbon nitride after carbon nitride synthesis. Tian and co-workers [33] adopted a wet-chemical “precursor preselection” strategy. The Fe₂-C₃N₄ catalyst was synthesized by using a dicarbonyl-cyclopentadienyl iron molecular precursor as an iron resource, mixed with the mesoporous C₃N₄ carrier using DMF as the solvent, and then calcined again at a high temperature. Obviously, this synthesis method, which required secondary calcination, also results in higher energy consumption. Despite extensive efforts, it is still challenging to find a simple and low-energy method to prepare single-atom catalysts.

Here, a simple and low-energy-consumption method was adopted. This study used Fe(acac)₃ (iron acetylacetonate) as the precursor, firstly adsorbed on g-C₃N₄ in solution, and then used NaBH₄ as the reducing agent to prepare a Fe single-atom catalyst (Fe-SACs/g-C₃N₄) successfully. The morphology, composition, and optical properties of the synthesized samples were characterized by SEM, STEM, ATR-FTIR, UV-vis, and PL. The coordination form of Fe single atoms in carbon nitride was analyzed by XPS and EXAFS, and the electron transfer changes of Fe single atoms anchored in carbon nitride were calculated by density functional theory (DFT). The photocatalytic performance and stability were evaluated by the degradation of 2-mercaptobenzothiazole (MBT) under visible light irradiation. Furthermore, a possible photocatalytic mechanism is proposed based on the results of EPR and the experimental results of trapping active species. Finally, the intermediates of MBT degradation were determined by LC-MS, and the degradation pathway of MBT was proposed. This research will provide promising solutions for the treatment of environmental pollutants and ideas for the rational design of high-performance single-atom catalysts.

2. Results and Discussion

2.1. Morphology and Crystal Structure

The morphology and microstructure information of the as-prepared samples were studied using SEM and TEM images. Figure 1a–c show the SEM images of $g\text{-C}_3\text{N}_4$, $\text{Fe}(\text{acac})_3/g\text{-C}_3\text{N}_4$, and $\text{Fe-SACs}/g\text{-C}_3\text{N}_4$, respectively. It can be seen that the materials are in a stacked layered structure; no aggregated Fe species were found on the surface of the $\text{Fe}(\text{acac})_3/g\text{-C}_3\text{N}_4$ and $\text{Fe-SACs}/g\text{-C}_3\text{N}_4$ samples. High-resolution TEM (HR-TEM) (Figure 1d) also shows that no Fe particles were observed in $\text{Fe-SACs}/g\text{-C}_3\text{N}_4$, and no obvious lattice fringes were found, proving the amorphous state of $\text{Fe-SACs}/g\text{-C}_3\text{N}_4$, which suggested that Fe might only be connected to the unsaturated coordinating N atom in the tri-s-triazine unit [34]. This is also consistent with the test results of XRD. Aberration-corrected high-angle annular dark-field scanning TEM (AC-HAADF-STEM) images (Figure 1e,f) further confirm that there are no agglomerated Fe nanoparticles in $\text{Fe-SACs}/g\text{-C}_3\text{N}_4$; uniformly dispersed single-atom-sized bright spots can be observed, and thus Fe single atoms are uniformly dispersed in the $g\text{-C}_3\text{N}_4$ nanosheets. At the same time, the result of the element mapping image (Figure 1g) also shows that C, N, O, and Fe elements are uniformly distributed in $g\text{-C}_3\text{N}_4$. According to the ICP test, the Fe content of the 2% $\text{Fe-SACs}/g\text{-C}_3\text{N}_4$ sample is approximately 0.1 wt% (Table S1).

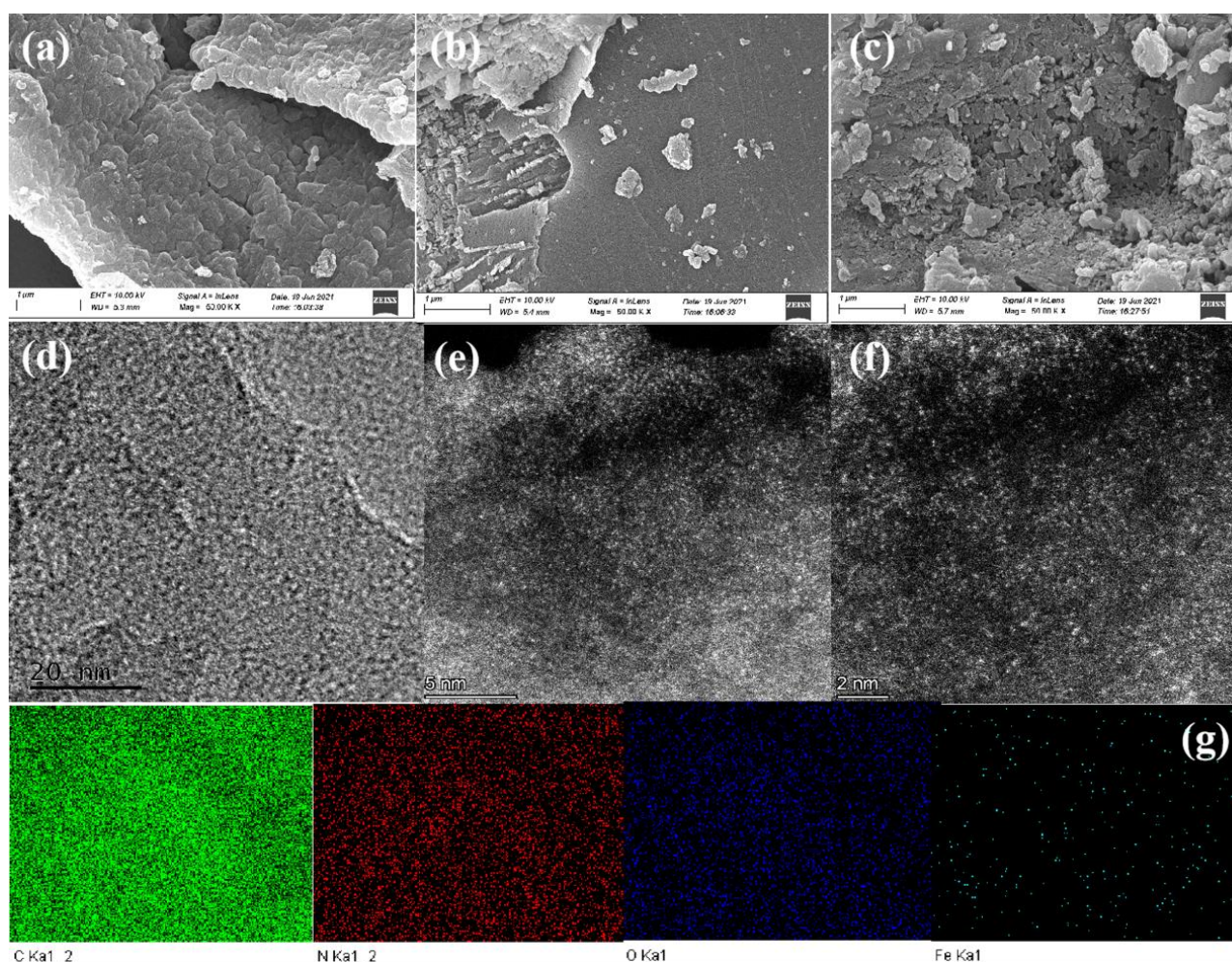


Figure 1. SEM images of $g\text{-C}_3\text{N}_4$ (a) $\text{Fe}(\text{acac})_3/g\text{-C}_3\text{N}_4$ (b), and $\text{Fe-SACs}/g\text{-C}_3\text{N}_4$ (c); TEM image of $\text{Fe-SACs}/g\text{-C}_3\text{N}_4$ (d); HAADF-STEM images of $\text{Fe-SACs}/g\text{-C}_3\text{N}_4$ (e–f); and the corresponding element mappings for the C (Green), N (Red), O (Blue) and Fe (cyan-blue) atoms of $\text{Fe-SACs}/g\text{-C}_3\text{N}_4$ (g).

Figure 2a displays the XRD patterns of $g\text{-C}_3\text{N}_4$, $\text{Fe}(\text{acac})_3/g\text{-C}_3\text{N}_4$, and $\text{Fe-SACs}/g\text{-C}_3\text{N}_4$, respectively. The stronger peak, which corresponds to the (002) crystal plane at 27.4° , represents the characteristic interlayer stacking reflection of conjugated aromatic systems. The weaker peak is at 13.1° , and corresponds to the (100) crystal plane [35]. It represents the in-plane structural orderly stacking of tri-s-triazine units. It can be seen that the peak intensity changes slightly after adding $\text{Fe}(\text{acac})_3$, probably because $\text{Fe}(\text{acac})_3$ is only adsorbed on the surface of $g\text{-C}_3\text{N}_4$ and has little effect on the structure of $g\text{-C}_3\text{N}_4$, and with the reduction, Fe atoms enter the $g\text{-C}_3\text{N}_4$ framework. The peak at 27.4° decreases, which indicates the host-guest interaction and the inhibition of polymer condensation by excessive Fe species [36]. The full width at half maxima (FWHM) data and the crystallite size of the (002) peak show that with the addition of single atom Fe, the half-peak width of the (002) crystal plane of carbon nitride material was expanding and the crystallite size was decreasing (Table S2). The Fe peak was not detected, which may be due to the low concentration and uniform dispersion of Fe in $g\text{-C}_3\text{N}_4$ [37].

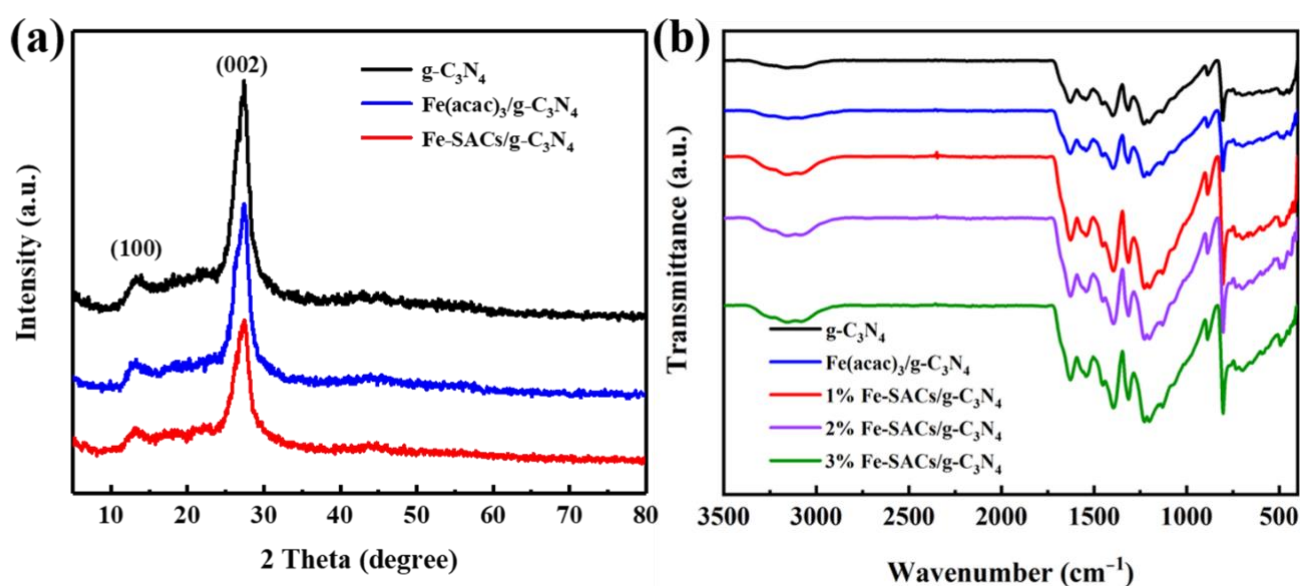


Figure 2. XRD patterns of $g\text{-C}_3\text{N}_4$, $\text{Fe}(\text{acac})_3/g\text{-C}_3\text{N}_4$, and $\text{FeSACs}/g\text{-C}_3\text{N}_4$ (a); FTIR spectra of $g\text{-C}_3\text{N}_4$, $\text{Fe}(\text{acac})_3/g\text{-C}_3\text{N}_4$, and $\text{FeSACs}/g\text{-C}_3\text{N}_4$ (b).

To further study the chemical bonding and chemical structure of the prepared samples, Fourier Transform Infrared (FT-IR) studies were carried out. The FT-IR spectra of the samples are shown in Figure 2b. The absorption in the range of $3050\text{--}3450\text{ cm}^{-1}$ can be attributed to the amino vibrations, the multiple peaks in the range of $1200\text{--}1680\text{ cm}^{-1}$ can be attributed to the CN heterocyclic [38], and the peak at 809 cm^{-1} can correspond to the breathing mode of triazine units [39]. The basic framework of carbon nitride is unchanged, which is due to the introduction of a trace amount of Fe into the framework.

Figure S1 shows the N_2 adsorption and desorption isotherm curves. The N_2 adsorption curves of the samples are all type IV H_3 hysteresis curves. According to the literature, the relative pressure range of a H_3 hysteresis curve is 0.65–0.95, and these curves are typical slit-shaped mesopores [40]. In accordance with the test results, the specific surface area and pore diameter of the materials were calculated using the BET method and the BJH method. The specific surface area of $\text{Fe-SACs}/g\text{-C}_3\text{N}_4$ was $7.80\text{ m}^2/\text{g}$, which was slightly higher than the $7.72\text{ m}^2/\text{g}$ specific surface area of $g\text{-C}_3\text{N}_4$. The increase in the specific surface area of $g\text{-C}_3\text{N}_4$ may be due to the influence of Fe doping on the crystallinity of $g\text{-C}_3\text{N}_4$. A higher specific surface area means more active centers and more sufficient contact between the catalyst and the pollutants, thereby improving the photocatalytic activity. The average pore diameter of $g\text{-C}_3\text{N}_4$ is 19.45 nm, and that of $\text{Fe-SACs}/g\text{-C}_3\text{N}_4$ is 17.76 nm, which indicates that the material has a mesoporous (2–50 nm) structure [41].

The chemical state and chemical composition of Fe-SACs/g-C₃N₄ samples were measured by X-ray photoelectron spectroscopy (XPS). Figure 3a is the full spectrum of the catalyst element. C, N, and O were detected respectively. Specifically, the high-resolution C 1s XPS of Fe-SACs/g-C₃N₄ (Figure 3b) has four distinct peaks: among them, 284.6 eV belongs to adventitious carbon (C-C), and 286.4 eV belongs to the sp³-hybridized carbon (C-(N)₃). The peak at 288.4 eV is attributed to the sp²-hybridized carbon (N-C=N), and the peak at 293.2 eV is assigned to the π - π^* satellite structure [42]. The N 1s spectra (Figure 3c) have four peaks centered at 398.5 eV, which are assigned to the sp²-hybridized nitrogen in aromatic triazine rings (C-N=C), usually called pyridine nitrogen. The peak at 399.8 eV belongs to the tertiary nitrogen (N-(C)₃), 400.9 eV is attributed to the free amino groups (C-N-H), and 404.2 eV belongs to the charging effects or positive charge localization in the heterocycles [43]. It is worth noting that compared with g-C₃N₄, the binding energy of pyridine nitrogen in the Fe-SACs/g-C₃N₄ catalyst has shifted, which may be due to the combination of Fe and pyridine nitrogen, and the content of pyridine nitrogen has also increased, which is more conducive to the binding with Fe atom [37]. In other words, the electron density of pyridine N atoms is slightly reduced due to their interaction with Fe atoms. Therefore, it can be concluded that Fe atoms in carbon nitride are mainly stabilized by pyridine N atoms [44], which may be formed in coordination with Fe and become a new electron transfer channel. However, as the binding energy of Fe(acac)₃/g-C₃N₄ does not shift in comparison to g-C₃N₄, we speculate that when NaBH₄ is not added for reduction, the Fe in Fe(acac)₃ is still connected to the ligand, not bonded to carbon nitride, and is only adsorbed on the surface of carbon nitride. After reduction, the positive charge of the iron atom disappeared, and then the interaction with acetylacetonate negative ions became weak. Meanwhile, the coordination interaction between the iron and the pyridine nitrogen increased, so the iron stabilized in carbon nitride. Due to the low iron content of the 2% Fe-SACs/g-C₃N₄ sample (Figure 3d), high-resolution XPS spectra of Fe were not detected.

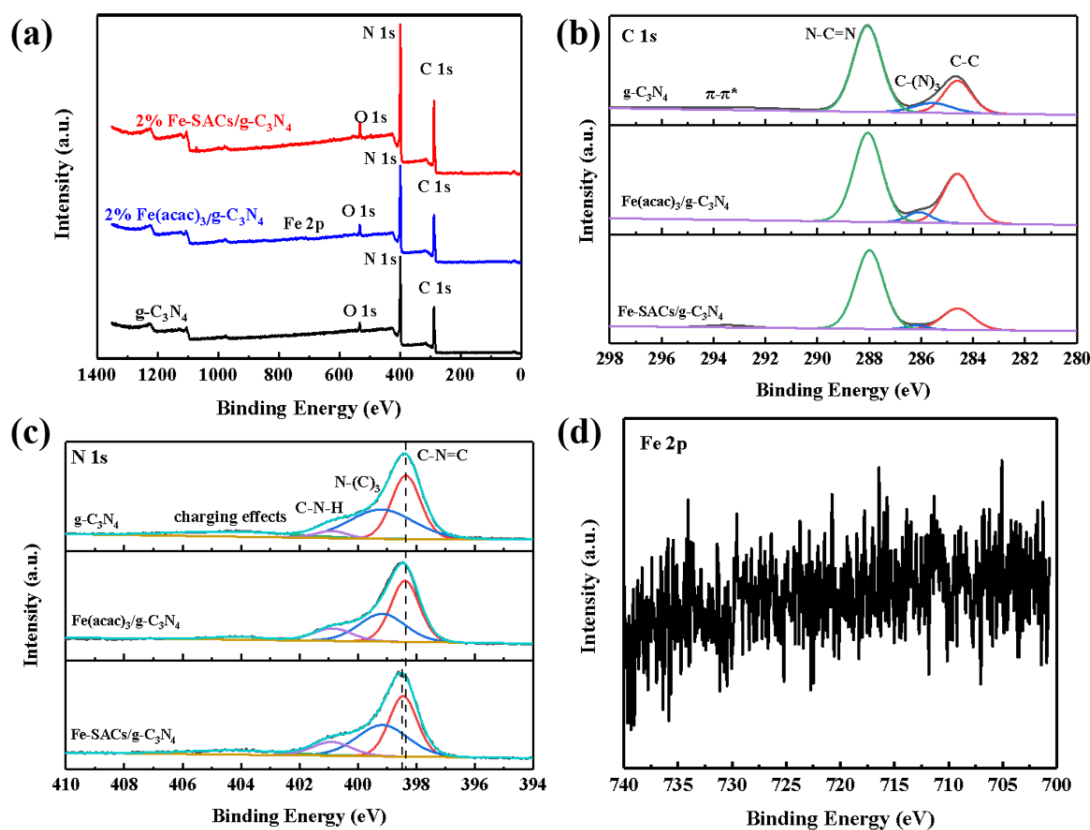


Figure 3. Full XPS spectra of g-C₃N₄, Fe(acac)₃/g-C₃N₄, and 2% Fe-SACs/g-C₃N₄ (a); and high-resolution XPS spectra of 2% Fe-SACs/g-C₃N₄ C 1s (b), N 1s (c), and Fe 2p (d).

The atomic local structure information and coordination of Fe-SACs/g-C₃N₄ were studied using X-ray absorption fine structure (XAFS) spectroscopy and extended XAFS (EXAFS) measurement. The Fe K-edge X-ray absorption near-edge structure spectrum of Fe-SACs/g-C₃N₄ (Figure 4a) shows that with the increase in the Fe element valence, the rising edge gradually moves to the higher energy region. The rising edge position of Fe-SACs/g-C₃N₄ is between the FeO and Fe₂O₃, indicating that a single Fe atom is positively charged between +2 and +3 valence [45]. From the quantitative EXAFS fittings (Table S3), the coordination characteristic of Fe-SACs/g-C₃N₄ to Fe-N is 4.2, indicating the presence of predominant single Fe atoms in Fe-SACs/g-C₃N₄. The FT k³-weighted $\chi(k)$ function EXAFS spectrum (Figure 4b) of Fe-SACs/g-C₃N₄ did not match the main peak of Fe foil at ~ 2.2 Å, indicating no obvious iron-iron bonding [46]. This further demonstrates the atomic dispersion of Fe in the Fe-SACs/g-C₃N₄ catalyst. The dominant peak at ~ 1.5 Å can be attributed to Fe-N coordination [47]. Furthermore, the WT contour plot of Fe-SACs/g-C₃N₄ showed an intensity maximum at ~ 4.2 Å⁻¹ (Figure 4c). In Fe-SACs/g-C₃N₄, no maximum intensity of ~ 7.1 Å⁻¹ associated with Fe-Fe linkages was observed, suggesting that in the as-prepared catalysts, dispersed Fe is dominated by Fe atoms. To obtain quantitative structural parameters of Fe in Fe-SACs/g-C₃N₄ catalysts, we performed least-squares EXAFS curve fitting. (Figure S2) The results show that the Fe-N_x coordination number of the Fe-SACs/g-C₃N₄ catalyst is 4. Moreover, the coordination characteristics show that all Fe sites in Fe-SACs/g-C₃N₄ can be assigned as Fe single atoms. The single-atom iron reduced by NaBH₄ was not stable and would be oxidized to an iron positive ion after coordinating with g-C₃N₄.

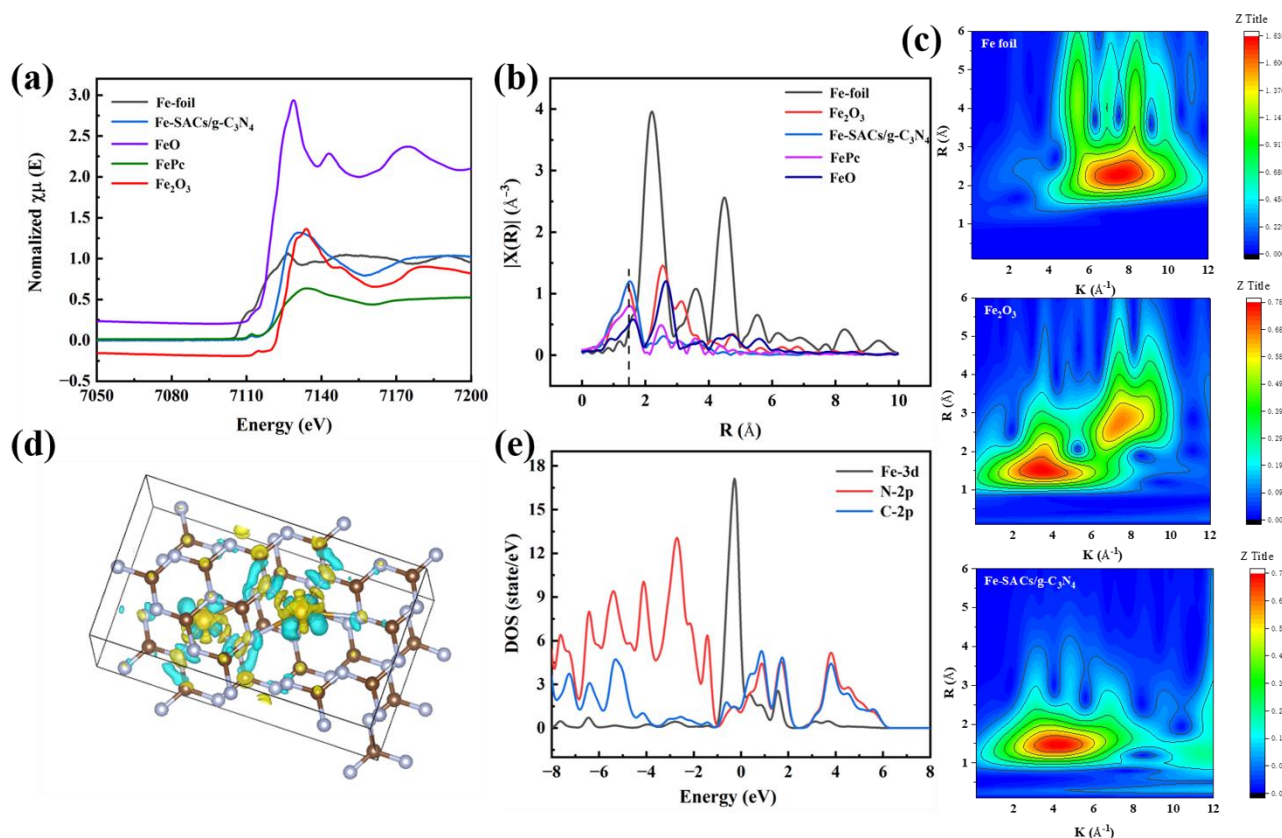


Figure 4. (a) XANES spectra at the Fe Kedge of FeSACs/gC₃N₄ and reference samples; (b) FT k³weighted EXAFS spectra of FeSACs/gC₃N₄ and reference samples; (c) WT plot of Fe-SACs/g-C₃N₄; (d) Differential charge density of the Fe-N₄ coordination systems (The blue regions illustrate charge depletion while the green regions indicate charge accumulation); (e) Density of states of the Fe-N₄ coordination systems.

To further demonstrate the electronic structure of Fe-SACs/g-C₃N₄, we performed density functional theory (DFT) calculations. Using differential charge density to analyze the interaction between Fe-N₄ sites (Figure 4d), it was observed that most of the charge transfer occurred between Fe and N. The interaction between Fe and C is weak because there is no obvious charge transfer between Fe and C. This charge redistribution can generate more charge transfer around the Fe single-atom sites and more catalytic active sites to effectively degrade MBT. Moreover, as can be seen from the projected density of states (DOS) curves (Figures 4e and S3), these bonds are formed by the interaction of Fe 3d with N 2p orbitals, further confirming the formation of in-plane bonds, which may lead to the formation of in-plane electron transfer improvements.

2.2. Optical and Photoelectrochemical Properties

The PL spectra of g-C₃N₄, Fe(acac)₃/g-C₃N₄, and Fe-SACs/g-C₃N₄ were measured at an excitation wavelength of 355 nm, as shown in Figure 5a. A broad peak of pristine g-C₃N₄ was observed at 470 nm with the highest peak intensity, indicating an increased rate of carrier recombination. In addition, with the introduction of Fe(acac)₃, a slight increase in fluorescence was observed. This may be due to the adsorption of Fe(acac)₃ by a g-C₃N₄ that reduces the thermal vibration of the molecule and, as Fe(acac)₃ contains the fluorophore C=O, this results in an increased fluorescence intensity [48]. Among all the samples, the Fe-SACs/g-C₃N₄ composite has the lowest photoluminescence intensity, which indicates that the photogenerated electron/hole separation is the most efficient. Therefore, the introduction of Fe atoms to the g-C₃N₄ structure facilitates the separation of photogenerated electron-hole pairs in g-C₃N₄, which can effectively inhibit the recombination of photogenerated carriers [49].

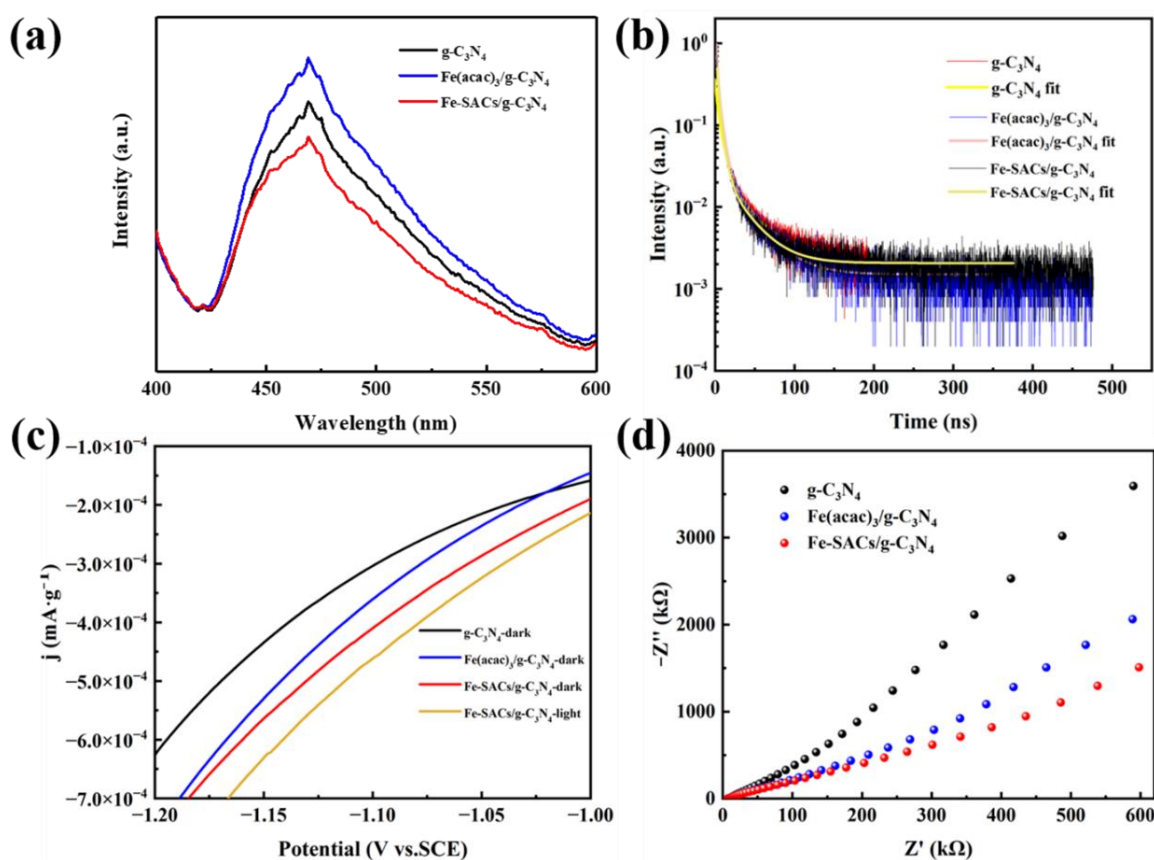


Figure 5. PL spectra of photocatalysts (a); Time-resolved photoluminescence decay traces (b); LSV curves (c); Nyquist plots of EIS (d).

Time-resolved photoluminescence (TRPL) decay experiments provide a more detailed understanding of the carrier transfer kinetics of the catalyst (Figure 5b). The TRPL decay spectrum curve fitted with exponential decay kinetic function expressed as Equation (1)

$$I(t) = A_1(\exp^{-t/\tau_1}) + A_2(\exp^{-t/\tau_2}) + A_3(\exp^{-t/\tau_3}). \quad (1)$$

At the same time, the average emission lifetime (τ_A), which reflects the overall emission decay behavior, is calculated using Equation (2)

$$\tau_A = (A_1\tau_1^2 + A_2\tau_2^2 + A_3\tau_3^2)/(A_1\tau_1 + A_2\tau_2 + A_3\tau_3). \quad (2)$$

In this equation, τ_1 , τ_2 , and τ_3 are the emission lifetimes, τ_1 is caused by free exciton recombination, and τ_2 and τ_3 are caused by nonradiative recombination of surface defect states charge carriers [50], and A_1 , A_2 , and A_3 are the corresponding amplitudes. As shown in Table 1, the fluorescence lifetime of g-C₃N₄ decays from 13.1 ns to 9.4 ns (Fe(acac)₃/g-C₃N₄), and finally to 7.6 ns (Fe-SACs/g-C₃N₄), revealing the existence of a more efficient carrier dissociation and migration process [51]. This also proves that there are new electron transfer channels, and the electron transfer rate is accelerated. It can be seen that the τ_1 of (Fe(acac)₃/g-C₃N₄) is slightly larger than that of g-C₃N₄, which is also consistent with the phenomenon in PL.

Table 1. Kinetic parameters of time-resolved fluorescence decays of g-C₃N₄, Fe(acac)₃/g-C₃N₄, and Fe-SACs/g-C₃N₄ under 470 nm excitation.

Sample	τ_1	A_1	τ_2	A_2	τ_3	A_3	τ_{average}
g-C ₃ N ₄	1.7126	0.376	7.0426	0.429	48.0688	0.195	36.284
Fe(acac) ₃ /g-C ₃ N ₄	1.7263	0.449	7.2545	0.446	51.4631	0.105	32.222
Fe-SACs/g-C ₃ N ₄	1.4582	0.451	6.2043	0.451	41.9526	0.098	25.248

Figure 5c shows the comparison of g-C₃N₄, Fe(acac)₃/g-C₃N₄, and Fe-SACs/g-C₃N₄ LSV curves in the potential window from −1.2 to −1.0 V. Obviously, the photocurrent density of Fe-SACs/g-C₃N₄ is higher than that of g-C₃N₄ and Fe(acac)₃/g-C₃N₄. Additionally, for the same material, the current density is significantly higher in light conditions than in dark conditions. The increased photocurrent response implies that the separation of photogenerated charge carriers is increased [52]. Figure S4 compares the photocurrent response generated by g-C₃N₄ and Fe-SACs/g-C₃N₄ in 0.5 M sodium sulfate solution. It can be seen that Fe-SACs/g-C₃N₄ shows the maximum photocurrent density compared with g-C₃N₄ when illuminated. In order to further explore the separation and transfer of photogenerated carriers, electrochemical impedance spectroscopy (EIS) tests were carried out in the electrochemical workstation [53]. Figure 5d shows the electrochemical impedance spectroscopy (EIS) Nyquist plot of g-C₃N₄, Fe(acac)₃/g-C₃N₄, and Fe-SACs/g-C₃N₄. Since the preparation of the electrode and the electrolyte is the same, the semicircle is related to the resistance of the electrode. The arc radius on the EIS-Nyquist diagram of Fe-SACs/g-C₃N₄ is smaller than that of the original g-C₃N₄ and Fe(acac)₃/g-C₃N₄. This indicates that the former has more effective photo-generated electron pair separation and faster interface charge transfer [54]. This phenomenon also proves that a new electron transfer channel is generated.

The optical properties of the samples were studied using UV-vis diffuse reflectance spectroscopy, as shown in Figure 6a. It can be seen that the absorbance of g-C₃N₄ and Fe(acac)₃/g-C₃N₄ is not much different, but the absorbance of Fe-SACs/g-C₃N₄ is significantly improved, with 2% Fe-SACs/g-C₃N₄ being the highest. This shows that Fe-SACs/g-C₃N₄ can make full use of visible light and generate more effective photo-generated charge carriers, thus improving photocatalytic activity [55].

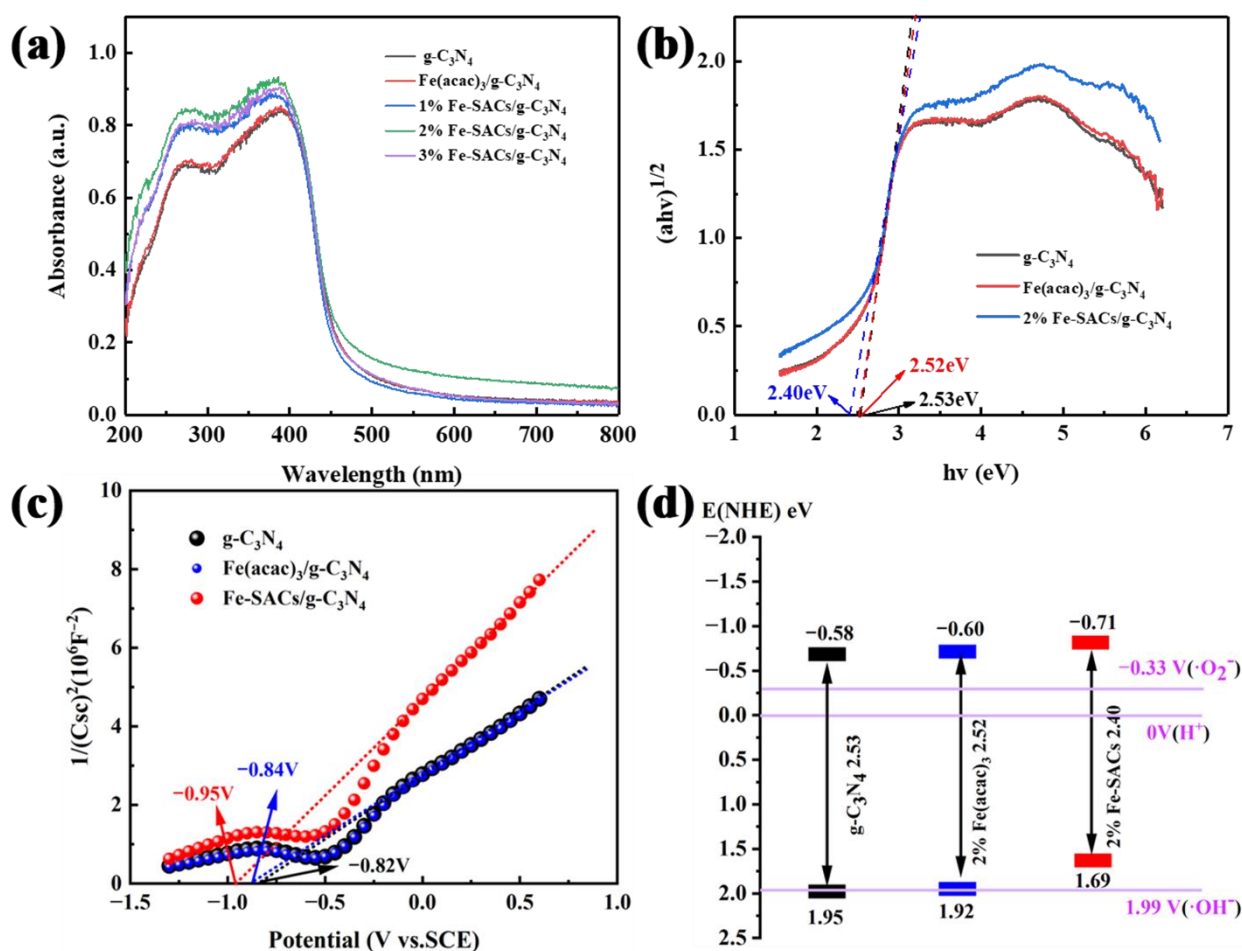


Figure 6. UVvis absorption spectrum (a); Tauc diagram of photocatalysts (b); Mott–Schottky curves (c); energy band diagram (d).

The bandgap energy is obtained by plotting the relationship between $(\alpha h\nu)^{1/2}$ and $h\nu$, where α is the absorption coefficient and $h\nu$ is the photon energy [56]. The Tauc diagram of the absorption data (Figure 6b) shows that the bandgap energy of Fe-SACs/g-C₃N₄ is 2.40 eV, which is lower than 2.52 eV of g-C₃N₄ and 2.53 eV of Fe(acac)₃/g-C₃N₄. It indicates that the adsorption of Fe(acac)₃ has little effect on the band gap of g-C₃N₄, while the addition of single-atom Fe is beneficial to reducing the band gap, thus significantly improving the photocatalytic activity.

The band structures of g-C₃N₄, Fe(acac)₃/g-C₃N₄, and Fe-SACs/g-C₃N₄ were studied by Mott–Schottky analysis. The positive slope of the Mott–Schottky diagram illustrates the n-type semiconductor characteristics of the material [57] as shown in Figure 6c. Therefore, the calculated CB of g-C₃N₄, Fe(acac)₃/g-C₃N₄, and Fe-SACs/g-C₃N₄ are −0.82, −0.84, and −0.95 V (vs. SCE), respectively, which are equal to −0.68, −0.70 and −0.71 V (vs. NHE) (Equation (3)), respectively. The band structures of these materials are shown in Figure 6d.

$$E \text{ (vs. SCE)} = E \text{ (vs. NHE)} - 0.24 \quad (3)$$

2.3. Photocatalytic Activity

The degradation of MBT by the material under visible light irradiation was investigated. Figure 7a compares the photocatalytic activity of the carbon nitride samples before and after modification. Due to the high recombination rate of electrons and holes and the insufficient use of visible light, the activity of g-C₃N₄ is poor. After 35 min of visible light irradiation, only 42% of MBT was removed. The activity was slightly enhanced after Fe(acac)₃ was adsorbed, and 54% of MBT was degraded after 35 min. However, after

Fe-SACs were incorporated, the activity was greatly enhanced, and the degradation rate reached 99% within 35 min. When the incorporation ratio of Fe-SACs was less than 2%, the presence of Fe-SACs in the photocatalyst improved the catalytic activity and reduced the recombination rate of photo-induced carriers. However, when the Fe-SACs doping amount was greater than 2%, its catalytic activity remains basically unchanged or even slightly decreased, which may be related to the formation of new recombination centers by the excessive iron. In order to gain insight into the process of degradation reactions, the reaction rate constants were calculated according to the following first-order model (Equation (4)).

$$-\ln(C/C_0) = kt \quad (4)$$

where C is the residual concentration at reaction time (t), C_0 is the initial concentration of MBT after establishing adsorption-desorption equilibrium, and k is the first-order rate constant [58].

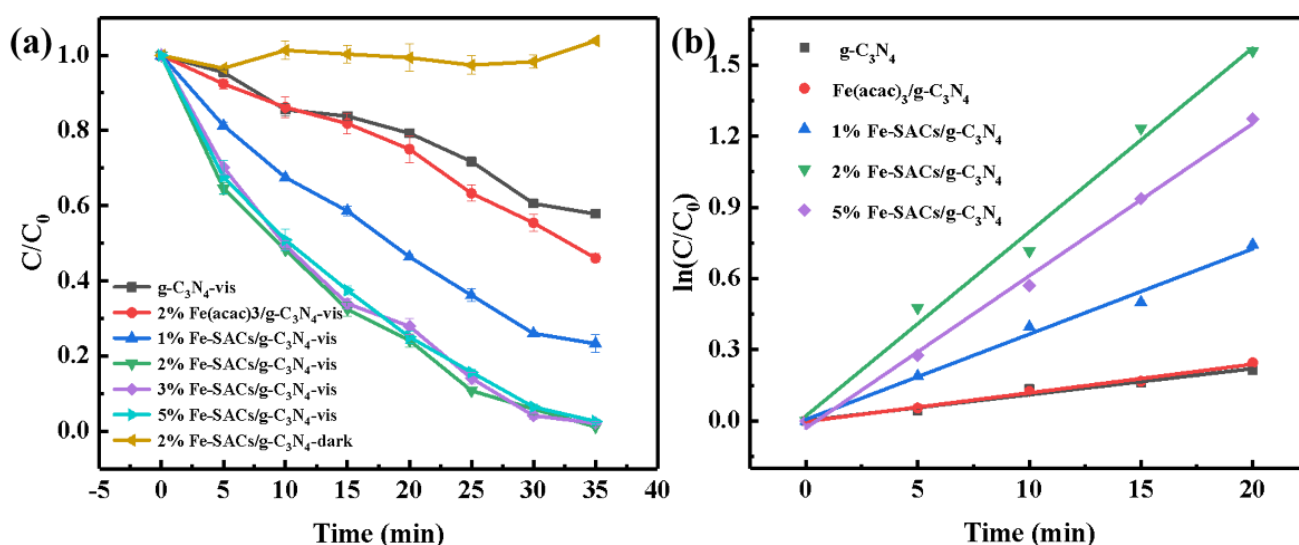


Figure 7. (a) Photocatalytic MBT removal ratio by various photocatalysts; (b) Pseudo-first-order kinetics over materials.

As shown in Figure 7b, the photocatalytic degradation kinetics of the as-prepared 2% Fe-SACs/ $g-C_3N_4$ had a maximum rate constant of 0.078 min^{-1} , which was 6.5 and 7.1 times higher than those of $Fe(acac)_3/g-C_3N_4$ (0.012 min^{-1}) and $g-C_3N_4$ (0.011 min^{-1}) (Figure S5). The UV-Vis spectral changes of MBT during photoreaction are shown in Figure S6.

The stability of photocatalyst in the experiment is an important parameter in its practical application. Therefore, we tested the cyclic degradation performance of the as-prepared Fe-SACs/ $g-C_3N_4$ for MBT, and the results are shown in Figure 8a. During the five degradation cycles, there was no significant drop in efficiency. In addition, we also investigated the physical structure and optical capabilities of the fresh and used Fe-SACs/ $g-C_3N_4$ photocatalysts using FTIR and UV-vis (Figure 8b,c). The used catalyst has no change in morphology (Figure S7). The results showed that the physical and optical properties of Fe-SACs/ $g-C_3N_4$ did not change much after the reaction, indicating that the prepared Fe-SACs/ $g-C_3N_4$ photocatalyst had good stability.

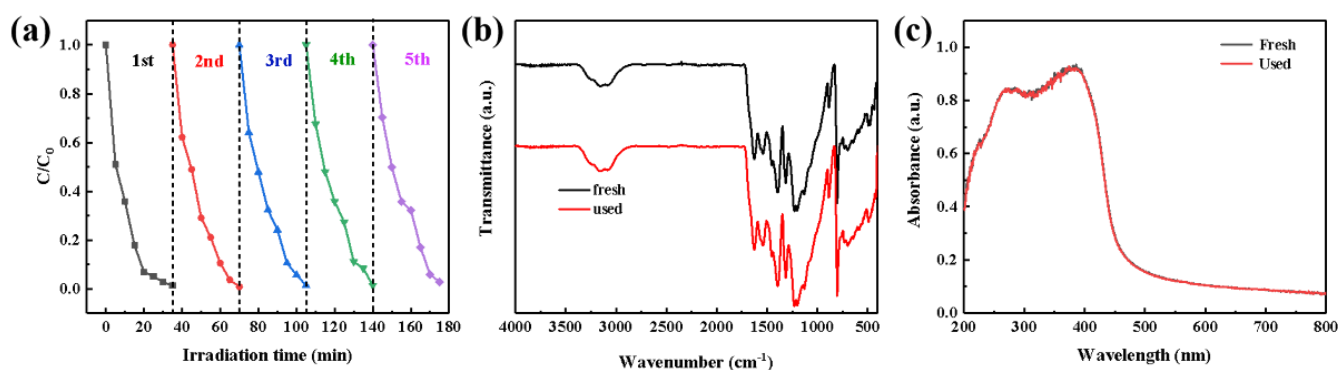


Figure 8. (a) Degradation performance of Fe-SACs/g-C₃N₄ toward MBT over five cycles; (b) FT-IR; and (c) UV-vis spectra of fresh and used Fe-SACs/g-C₃N₄ photocatalyst.

2.4. Degradation Mechanism Analysis

The main reactive species in the Fe-SACs/g-C₃N₄ photocatalytic reaction were studied by trapping experiments. It can be seen from Figure 9a that when ethanol (EA) (10 mmol/L) was introduced into the reaction solution, the degradation curve of MBT did not change significantly, indicating that $\cdot\text{OH}$ did not contribute substantially to the degradation reaction of MBT. The introduction of disodium ethylenediaminetetraacetate (EDTA-2Na) (10 mmol/L) slightly inhibited the degradation curve of MBT, which indicated that holes were involved in the photocatalytic degradation process of MBT. However, the degradation rate of MBT was greatly inhibited when nitroxide radical piperidinol (TEMPOL) (10 mmol/L) was added, indicating that $\cdot\text{O}_2^-$ is the main reactive species for the degradation of MBT in the Fe-SACs/g-C₃N₄ reaction system. Therefore, it can be inferred that the superoxide and holes generated in the photocatalytic reaction are responsible for the enhanced photooxidative performance of MBT decomposition. The same capture experiments were performed for g-C₃N₄ and Fe(acac)₃/g-C₃N₄, and the reactive species were the same as for Fe-SACs/g-C₃N₄ (Figure S8).

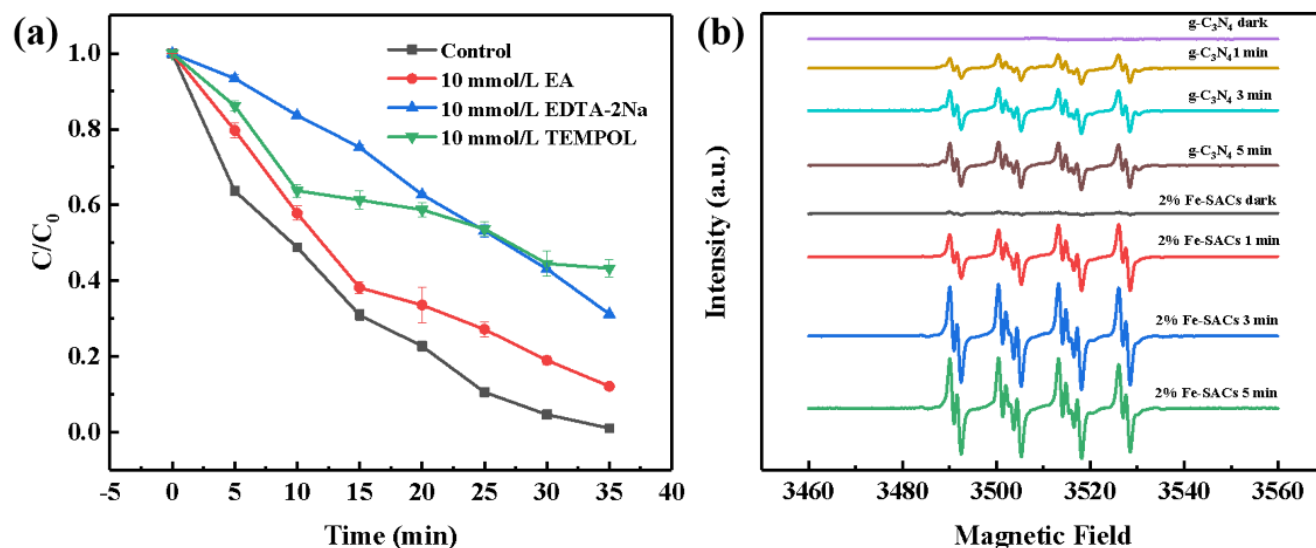


Figure 9. (a) The photocatalytic activity of Fe-SACs/g-C₃N₄ for degrading MBT with the presence of various scavengers; (b) the EPR spectrum of DMPO·O₂⁻ in the presence of g-C₃N₄ and Fe-SACs/g-C₃N₄.

To further determine the free radical generation obtained above, the presence of $\cdot\text{O}_2^-$ during the photodegradation reaction was confirmed using the EPR technique at room temperature (Figure 9b). Under dark conditions there is no signal, while the characteristic

peak of $\cdot\text{O}_2^-$ can be clearly observed under visible light. It can be seen that the signal of Fe-SACs/g- C_3N_4 is significantly stronger than that of g- C_3N_4 , indicating that the new electron transfer channel mediated by Fe single atoms accelerates the electron transfer rate, which helps to generate more $\cdot\text{O}_2^-$. Moreover, $\cdot\text{O}_2^-$ increases rapidly with the increase in illumination time, and the signal will gradually weaken under a longer illumination time. No signal of $\cdot\text{OH}$ was detected (Figure S9).

Based on the above experimental and characterization results, we propose a possible photocatalytic mechanism to explain the degradation process of MBT by Fe single-atom doped g- C_3N_4 composites (Figure 10). Under visible light activation, the electrons and holes in Fe-SACs/g- C_3N_4 are rapidly separated, the electrons are transferred to the conduction band (CB) and migrate to the iron species, while the holes stay in the valence band (VB), and then directly oxidize the contamination. Subsequently, electrons in Fe-SACs/g- C_3N_4 may be trapped by oxygen molecules, resulting in $\cdot\text{O}_2^-$, a powerful oxide species that can decompose MBT into small molecules. Therefore, the photodegradation reaction of the as-prepared Fe-SACs/g- C_3N_4 composites can improve the separation and transfer of photogenerated e^-/h^+ pairs, and has a strong photo-redox ability for the efficient decomposition of MBT.

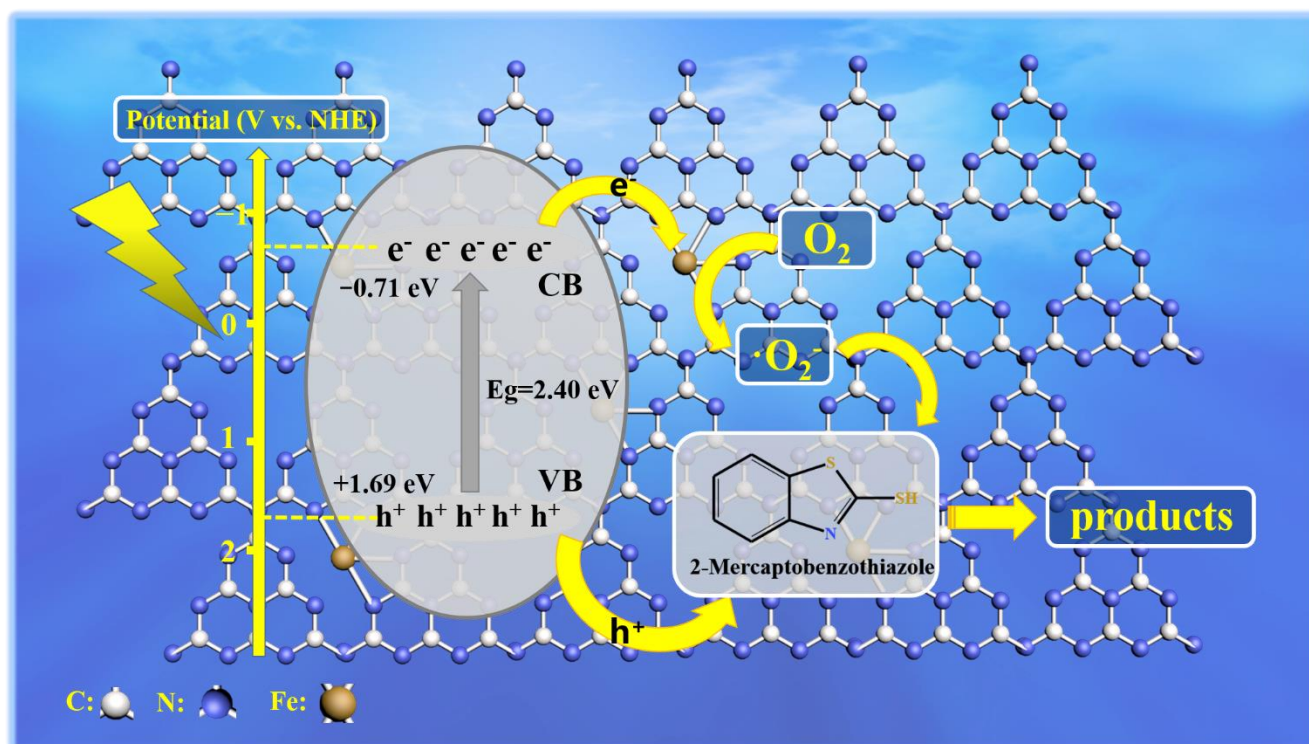


Figure 10. Schematic illustration of proposed catalytic mechanism in the Fe-SACs/g- C_3N_4 system.

2.5. Product Analysis

To study the degradation intermediates in the process of Fe-SACs/g- C_3N_4 photocatalytic degradation of MBT, high-performance liquid chromatography–mass spectrometry technology was used. Figure 11 showed the possible degradation pathways of MBT. First, MBT ($m/z = 167$) undergoes an addition reaction to produce compound B ($m/z = 169$) [59], then the $-\text{SH}$ group is lost to generate compound D ($m/z = 139$) [60], or MBT directly loses the $-\text{SH}$ group to generate C ($m/z = 135$) [61], and then the double bond is broken to generate compound D. With the progress of the reaction, compound D lost $-\text{CH}_3$ to form E ($m/z = 125$). Part of E is further decomposed to F ($m/z = 110$) by losing $-\text{NH}_2$ [62]. The other part is decomposed to G ($m/z = 93$) by losing $-\text{SH}$. Subsequently, compounds F and G were decomposed into H ($m/z = 114$) and I ($m/z = 95$), and finally degraded to J ($m/z = 82$) [63]. With the extension of the degradation time, MBT molecules may eventually

mineralize into CO_2 and H_2O . The corresponding mass spectrometry results are shown in Figure S10.

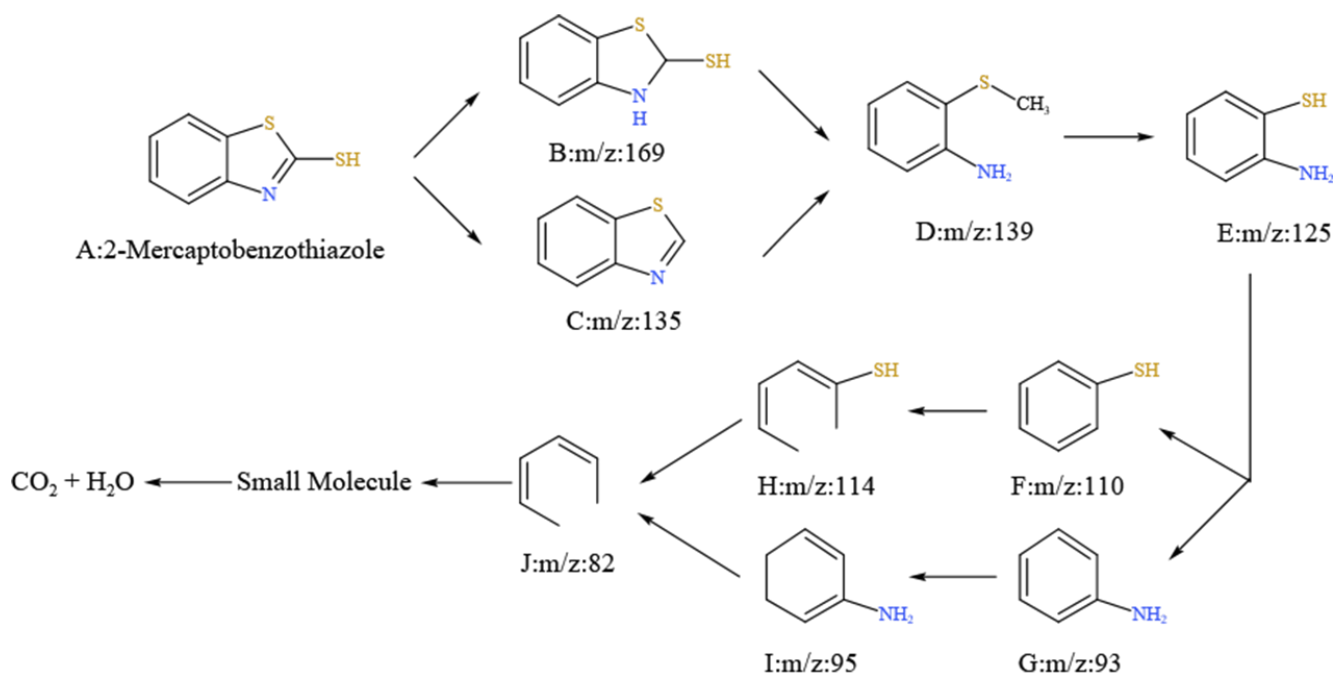


Figure 11. Possible transformation pathways of MBT degradation.

3. Experiment

3.1. Chemicals and Materials

All chemicals are analytical grade and require no further purification. Melamine ($\text{C}_3\text{H}_6\text{N}_6$, 99%) and iron acetylacetonate ($\text{Fe}(\text{acac})_3$, 98%) were purchased from McLean Reagent Company (Shanghai, China). Sodium borohydride (NaBH_4 , 98%) was purchased from Tianjin Damao Chemical Reagent Factory (Tianjin, China). Anhydrous ethanol ($\text{C}_2\text{H}_5\text{OH}$, $\geq 99.7\%$) was purchased from Fuyu Fine Chemical Reagent Co., Ltd. (Tianjin, China), and methanol (EA, $\geq 99.9\%$) was purchased from Tedia Company (Hefei, China). 2-Mercaptobenzothiazole (MBT, 98%), nitroxide radical piperidinol (TEMPOL), and disodium ethylenediaminetetraacetate (EDTA-2Na) were purchased from Aladdin Reagent Company (Shanghai, China). All aqueous solutions were prepared with deionized water.

3.2. Preparation of Catalyst

g- C_3N_4 : 10 g of melamine was put into a ceramic crucible with a lid, heated to 550°C at a heating rate of $5^\circ\text{C}/\text{min}$ in a muffle furnace, and calcined at this temperature for 4 h to obtain g- C_3N_4 .

$\text{Fe}(\text{acac})_3/\text{g-}\text{C}_3\text{N}_4$: 0.5 g of prepared g- C_3N_4 was dispersed in 20 mL of ethanol, different amounts of $\text{Fe}(\text{acac})_3$ (30 mg, 60 mg, 90 mg, 150 mg) were added to obtain a mixed solution, and the solution was then magnetically stirred at room temperature for 8 h. Afterward, the materials were washed with water and ethanol, respectively, dried at 60°C , and ground to obtain $\text{Fe}(\text{acac})_3/\text{g-}\text{C}_3\text{N}_4$.

Fe-SACs/g- C_3N_4 : 0.5 g $\text{Fe}(\text{acac})_3/\text{g-}\text{C}_3\text{N}_4$ with different Fe contents were dispersed in deionized water, 50 mg NaBH_4 was added, and the solution was stirred magnetically for three hours, then washed with water and ethanol, respectively, dried at 60°C , and then ground. Finally, Fe-SACs/g- C_3N_4 doped with different amounts of Fe were obtained. They were named 1% Fe-SACs/g- C_3N_4 , 2% Fe-SACs/g- C_3N_4 , 3% Fe-SACs/g- C_3N_4 , and 5% Fe-SACs/g- C_3N_4 , respectively.

3.3. Characterization Method

The phase composition and crystal structure of the prepared catalysts were analyzed using XRD ray diffraction (XRD, D/max2200PC, Rigaku, Osaka, Japan) using Cu-K α radiation. The morphology of the synthesized samples was investigated using scanning electron microscopy (SEM) on a Zeiss Sigma500 (Oberkochen, Baden-Württemberg, Germany), the microstructure of the catalyst was analyzed by transmission electron microscopy (TEM, FEI-F20, Hillsboro, OR, USA), and high-angle annular dark-field scanning transmission electron microscopy (HAADF-STEM) images were made using a FEI Themis Z (Hillsboro, OR, USA). The chemical states of surface elements were analyzed using X-ray photoelectron spectroscopy (XPS, Shimadzu Kratos AXIS SUPRA, Tokyo, Japan). Infrared spectra were recorded using a Fourier transform attenuated total reflection infrared spectrometer (ATR-FTIR, Bruker INVENIO-R, Saarbrücken, Germany). Nitrogen adsorption isotherms were acquired using an automatic gas adsorption analyzer (Mike ASAP2460, Atlanta, GA, USA) to evaluate their surface area and pore structure. Ultraviolet-visible diffuse reflectance spectroscopy (UV-vis DRS) data were acquired using a Cary 5000, Agilent, Santa Clara, CA, USA. The photoluminescence (PL) spectra of the samples were obtained with a fluorescence spectrometer (Edinburgh FS5, UK) at room temperature with an excitation wavelength of 355 nm. Linear scanning voltammetry (LSV) and electrochemical impedance spectroscopy (EIS) were performed in a three-electrode system using an electrochemical analyzer (Chen Hua CHI660E, Shanghai, China) with Hg/HgCl₂, Pt flakes, and prepared photoelectrodes, as reference electrodes, counter electrodes and working electrodes, respectively. The tests were performed in a standard three-electrode system using a 0.5 M sodium sulfate (pH = 6.8) solution. The electron spin resonance (ESR, Bruker E500, Karlsruhe, Germany) spectra of the samples were measured using 5,5-Dimethyl-1-pyrrolidine-N-oxide (DMPO) as a radical spin trapping reagent. The MBT product under photoexcitation time was identified by liquid chromatography-mass spectrometry (LC-MS). The LC-MS was equipped with a BHE C18 column (50 \times 2.1 mm i.d., 1.7 μ m) (Agilent Technologies, Santa Clara, CA, USA). The X-ray absorption discovery structure spectra (Fe-K edge) were collected at Spring-8. The storage ring of the BSRF was operated at 2.5 GeV with a maximum current of 250 mA. Data were collected in transmission mode using a Si (111) double-crystal monochromator with an ionization chamber. All spectra were collected under ambient conditions. In addition, DFT calculations were used to further understand the active sites of the catalytic process. DFT calculation uses VASP auxiliary calculation. The generalized gradient approximation (GGA) and (PBE) functional were used to deal with the exchange-correlation energy. In terms of geometric optimization, the electron self-consistent convergence criterion is 10^{-6} eV, and the electron self-consistent convergence criterion is 0.02 eV/Å. VESTA was used to visualize the differential charge density.

3.4. Photocatalytic Experiments

3.4.1. Degradation of MBT

The photocatalytic activity of all samples was detected using a UV cut filter (300 W, CEL-HXF300) ($\lambda \geq 420$ nm) as the light source. Typically, 30 mg of the prepared photocatalyst was added to the MBT solution (30 mL, 20 mg/L). Before the photocatalytic degradation test was carried out, the reaction solution was stirred for 30 min in the dark to reach the adsorption-desorption equilibrium. In the process of photoreaction, 1.0 mL of the reaction solution was taken at specific time intervals and filtered through a 0.22 μ m filter for subsequent assays. The distance between the suspension surface and the light source was kept at 15 cm during the whole experiment.

3.4.2. Cycle Experiment

The stability of 2% Fe-SACs/g-C₃N₄ composites was investigated by cycling experiments. MBT was degraded 5 times with 2% Fe-SACs/g-C₃N₄ samples. After each reaction, the catalyst was collected and separated with a filter extractor, washed four times with ethanol and water, and dried in an oven at 60 °C.

3.4.3. Trapping Experiments of Radicals

The main active species during the degradation process was investigated by free radical trapping experiments. In order to study the active species present in the degradation reaction, appropriate scavengers were added to the experimental solution. The scavengers used in this study included EDTA-2Na, TEMPOL, and EA, which were used to quench holes (h^+), superoxide radicals ($\cdot O_2^-$), and hydroxyl radicals ($\cdot OH$), respectively. The concentrations of EDTA-2Na, TEMPOL, and EA were all 10 mmol/L.

4. Conclusions

In conclusion, the Fe-SACs/g-C₃N₄ catalysts exhibit extremely high degradation activity towards MBT. Fe single-atom doped graphitic carbon nitride material was synthesized by a simple and low-energy method, and Fe was uniformly dispersed in the g-C₃N₄ structure in the form of single atoms. The Fe coordinated with pyridine nitrogen in carbon nitride to produce a new Fe-N₄ electron transfer channel, which further improved the carrier transport efficiency, produced more active radicals, and improved the degradation efficiency of the material for MBT. It was shown that 99% of MBT can be degraded in 35 min. According to EPR and active species trapping experiments, holes and $\cdot O_2^-$ are the main oxidizing species. The high stability of Fe-SACs/g-C₃N₄ was verified in the cyclic reaction experiments. The catalytic activity of MBT maintained a degradation efficiency close to the original level after five cycles, which may be due to the high dispersion as Fe-N₄ active sites in the g-C₃N₄.

Supplementary Materials: The following supporting information can be downloaded at: <https://www.mdpi.com/article/10.3390/catal13030619/s1>, Figure S1: N₂ adsorption-desorption isotherms of the g-C₃N₄ and Fe-SACs/g-C₃N₄ (a) BJH pore size distribution curves of as-prepared photocatalysts (b); Figure S2: The EXAFS R space fitting curves of Fe-SACs/g-C₃N₄; Figure S3: Projected density of states of the Fe-N₄ system; Figure S4: Photocurrent density of the g-C₃N₄ and Fe-SACs/g-C₃N₄; Figure S5: Degradation rate constants of different photocatalysts; Figure S6: UV-Vis spectral changes of MBT during photoreaction; Figure S7: SEM of used Fe-SACs/g-C₃N₄ photocatalyst; Figure S8: The photocatalytic activity of g-C₃N₄ (a), Fe(acac)₃/g-C₃N₄ (b) for degrading MBT with the presence of various scavengers; Figure S9: The EPR spectrum of DMPO- $\cdot OH$ in the presence of Fe-SACs/g-C₃N₄; Figure S10: LC-MS spectra of MBT intermediates in the degradation reaction with Fe-SACs/g-C₃N₄; Table S1: ICP Test Details; Table S2: The FWHM data and crystallite size of (002) peak; Table S3: Parameters of EXAFS fits for Fe-SACs/g-C₃N₄.

Author Contributions: Conceptualization, X.H. and C.Y.; methodology, X.H., C.Y. and Y.B.; investigation, C.Y. and X.H.; writing—original draft preparation, C.Y.; writing—review and editing, X.H.; supervision, X.H. and B.C.; project administration, X.H. and Y.L.; funding acquisition, X.H. All authors have read and agreed to the published version of the manuscript.

Funding: National Natural Science Foundation of China (no. 22176120, 22206118) and Shaanxi Thousand Talents Plan-Youth Program Scholars.

Data Availability Statement: Not applicable.

Acknowledgments: Generous support from the National Natural Science Foundation of China (no. 22176120), Shaanxi University of Science and Technology, and Shaanxi Thousand Talents Plan-Youth Program Scholars are acknowledged.

Conflicts of Interest: The authors declare no conflict of interest.

References

1. Johnson, A.C.; Jin, X.; Nakada, N.; Sumpter, J.P. Learning from the past and considering the future of chemicals in the environment. *Science* **2020**, *367*, 384–387. [CrossRef] [PubMed]
2. Zeng, G.; Chen, M.; Zeng, Z. Risks of neonicotinoid pesticides. *Science* **2013**, *340*, 1403. [CrossRef] [PubMed]
3. Larsen, T.A.; Hoffmann, S.; Luthi, C.; Truffer, B.; Maurer, M. Emerging solutions to the water challenges of an urbanizing world. *Science* **2016**, *352*, 928–933. [CrossRef] [PubMed]

4. Dong, H.; Zeng, G.; Tang, L.; Fan, C.; Zhang, C.; He, X.; He, Y. An overview on limitations of TiO₂-based particles for photocatalytic degradation of organic pollutants and the corresponding countermeasures. *Water Res.* **2015**, *79*, 128–146. [[CrossRef](#)]
5. Luo, S.; Liu, Y.; Zhu, Y.; Niu, Q.; Cheng, M.; Ye, S.; Yi, H.; Shao, B.; Shen, M.; Wen, X.; et al. Perspectives on palladium-based nanomaterials: Green synthesis, ecotoxicity, and risk assessment. *Environ. Sci. Nano* **2021**, *8*, 20–36. [[CrossRef](#)]
6. Ye, S.; Cheng, M.; Zeng, G.; Tan, X.; Wu, H.; Liang, J.; Shen, M.; Song, B.; Liu, J.; Yang, H.; et al. Insights into catalytic removal and separation of attached metals from natural-aged microplastics by magnetic biochar activating oxidation process. *Water Res.* **2020**, *179*, 115876. [[CrossRef](#)]
7. Zhu, Z.; Fan, W.; Liu, Z.; Yu, Y.; Dong, H.; Huo, P.; Yan, Y. Fabrication of the metal-free biochar-based graphitic carbon nitride for improved 2-mercaptobenzothiazole degradation activity. *J. Photochem. Photobiol. A Chem.* **2018**, *358*, 284–293. [[CrossRef](#)]
8. Luo, Y.; Lu, Z.; Jiang, Y.; Wang, D.; Yang, L.; Huo, P.; Da, Z.; Bai, X.; Xie, X.; Yang, P. Selective photodegradation of 1-methylimidazole-2-thiol by the magnetic and dual conductive imprinted photocatalysts based on TiO₂/Fe₃O₄/MWCNTs. *Chem. Eng. J.* **2014**, *240*, 244–252. [[CrossRef](#)]
9. Xie, K.; Fang, J.; Li, L.; Deng, J.; Chen, F. Progress of graphite carbon nitride with different dimensions in the photocatalytic degradation of dyes: A review. *J. Alloys Compd.* **2022**, *901*, 163589. [[CrossRef](#)]
10. Ma, W.; Dong, X.A.; Wang, Y.; He, W.; Zhang, W.; Liang, Y.; Wang, Y.; Fu, W.; Liao, J.; Dong, F. Highly enhanced photocatalytic toluene degradation and in situ FT-IR investigation on designed Sn-doped biocl nanosheets. *Appl. Surf. Sci.* **2022**, *578*, 152002. [[CrossRef](#)]
11. Chu, Y.; Zheng, X.; Fan, J. Preparation of sodium and boron co-doped graphitic carbon nitride for the enhanced production of H₂O₂ via two-electron oxygen reduction and the degradation of 2,4-DCP via photocatalytic oxidation coupled with Fenton oxidation. *Chem. Eng. J.* **2022**, *431*, 134020. [[CrossRef](#)]
12. Xu, L.; Liu, L. Piezo-photocatalytic fuel cell with atomic Fe@MoS₂ on CFC helical electrode has enhanced peroxymonosulfate activation, pollutant degradation and power generation. *Appl. Catal. B Environ.* **2022**, *304*, 120953. [[CrossRef](#)]
13. Masih, D.; Ma, Y.; Rohani, S. Graphitic C₃N₄ based noble-metal-free photocatalyst systems: A review. *Appl. Catal. B Environ.* **2017**, *206*, 556–588. [[CrossRef](#)]
14. Wang, W.; Niu, Q.; Zeng, G.; Zhang, C.; Huang, D.; Shao, B.; Zhou, C.; Yang, Y.; Liu, Y.; Guo, H.; et al. 1D porous tubular g-C₃N₄ capture black phosphorus quantum dots as 1D/0D metal-free photocatalysts for oxytetracycline hydrochloride degradation and hexavalent chromium reduction. *Appl. Catal. B Environ.* **2020**, *273*, 119051. [[CrossRef](#)]
15. Song, Q.; Li, J.; Wang, L.; Qin, Y.; Pang, L.; Liu, H. Stable single-atom cobalt as a strong coupling bridge to promote electron transfer and separation in photoelectrocatalysis. *J. Catal.* **2019**, *370*, 176–185. [[CrossRef](#)]
16. Zhao, G.-Q.; Zou, J.; Hu, J.; Long, X.; Jiao, F.-P. A critical review on graphitic carbon nitride (g-C₃N₄)-based composites for environmental remediation. *Sep. Purif. Technol.* **2021**, *279*, 119769. [[CrossRef](#)]
17. Sher, M.; Javed, M.; Shahid, S.; Hakami, O.; Qamar, M.A.; Iqbal, S.; Al-Anazy, M.M.; Baghdadi, H.B. Designing of highly active g-C₃N₄/Sn doped ZnO heterostructure as a photocatalyst for the disinfection and degradation of the organic pollutants under visible light irradiation. *J. Photochem. Photobiol. A Chem.* **2021**, *418*, 113393. [[CrossRef](#)]
18. Qamar, M.A.; Javed, M.; Shahid, S.; Iqbal, S.; Abubshait, S.A.; Abubshait, H.A.; Ramay, S.M.; Mahmood, A.; Ghaithan, H.M. Designing of highly active g-C₃N₄/Co@ZnO ternary nanocomposites for the disinfection of pathogens and degradation of the organic pollutants from wastewater under visible light. *J. Environ. Chem. Eng.* **2021**, *9*, 105534. [[CrossRef](#)]
19. Chen, X.; Zhang, J.; Fu, X.; Antonietti, M.; Wang, X. Fe-g-C₃N₄-catalyzed oxidation of benzene to phenol using hydrogen peroxide and visible light. *J. Am. Chem. Soc.* **2009**, *131*, 11658–11659. [[CrossRef](#)]
20. Di, Y.; Wang, X.; Thomas, A.; Antonietti, M. Making metal-carbon nitride heterojunctions for improved photocatalytic hydrogen evolution with visible light. *ChemCatChem* **2010**, *2*, 834–838. [[CrossRef](#)]
21. Yang, X.F.; Wang, A.; Qiao, B.; Li, J.; Liu, J.; Zhang, T. Single-atom catalysts: A new frontier in heterogeneous catalysis. *Accounts Chem. Res.* **2013**, *46*, 1740–1748. [[CrossRef](#)] [[PubMed](#)]
22. Liu, J.C.; Wang, Y.G.; Li, J. Toward rational design of oxide-supported single-atom catalysts: Atomic dispersion of gold on ceria. *J. Am. Chem. Soc.* **2017**, *139*, 6190–6199. [[CrossRef](#)]
23. Sun, J.-F.; Xu, Q.-Q.; Qi, J.-L.; Zhou, D.; Zhu, H.-Y.; Yin, J.-Z. Isolated single atoms anchored on N-doped carbon materials as a highly efficient catalyst for electrochemical and organic reactions. *ACS Sustain. Chem. Eng.* **2020**, *8*, 14630–14656. [[CrossRef](#)]
24. Fu, J.; Yu, J.; Jiang, C.; Cheng, B. g-C₃N₄-based heterostructured photocatalysts. *Adv. Energy Mater.* **2018**, *8*, 1701503. [[CrossRef](#)]
25. Liu, J. Catalysis by supported single metal atoms. *ACS Catal.* **2016**, *7*, 34–59. [[CrossRef](#)]
26. Liu, J.; Bunes, B.R.; Zang, L.; Wang, C. Supported single-atom catalysts: Synthesis, characterization, properties, and applications. *Environ. Chem. Lett.* **2017**, *16*, 477–505. [[CrossRef](#)]
27. Wang, L.; Huang, L.; Liang, F.; Liu, S.; Wang, Y.; Zhang, H. Preparation, characterization and catalytic performance of single-atom catalysts. *Chin. J. Catal.* **2017**, *38*, 1528–1539. [[CrossRef](#)]
28. Li, Y.; Kong, T.; Shen, S. Artificial photosynthesis with polymeric carbon nitride: When meeting metal nanoparticles, single atoms, and molecular complexes. *Small* **2019**, *15*, e1900772. [[CrossRef](#)]
29. Chen, Z.; Mitchell, S.; Vorobyeva, E.; Leary, R.K.; Hauert, R.; Furnival, T.; Ramasse, Q.M.; Thomas, J.M.; Midgley, P.A.; Dontsova, D.; et al. Stabilization of single metal atoms on graphitic carbon nitride. *Adv. Funct. Mater.* **2017**, *27*, 1605785. [[CrossRef](#)]

30. Cao, H.; Wang, J.; Kim, J.-H.; Guo, Z.; Xiao, J.; Yang, J.; Chang, J.; Shi, Y.; Xie, Y. Different roles of Fe atoms and nanoparticles on g-C₃N₄ in regulating the reductive activation of ozone under visible light. *Appl. Catal. B Environ.* **2021**, *296*, 120362. [\[CrossRef\]](#)
31. Liu, W.; Chen, Y.; Qi, H.; Zhang, L.; Yan, W.; Liu, X.; Yang, X.; Miao, S.; Wang, W.; Liu, C.; et al. A durable nickel single-atom catalyst for hydrogenation reactions and cellulose valorization under harsh conditions. *Angew. Chem. Int. Ed. Engl.* **2018**, *57*, 7071–7075. [\[CrossRef\]](#) [\[PubMed\]](#)
32. Feng, J.; Dou, M.; Zhang, Z.; Wang, F. Template-free synthesis of two-dimensional Fe/N codoped carbon networks as efficient oxygen reduction reaction electrocatalysts. *ACS Appl. Mater. Interfaces* **2018**, *10*, 37079–37086. [\[CrossRef\]](#) [\[PubMed\]](#)
33. Tian, S.; Fu, Q.; Chen, W.; Feng, Q.; Chen, Z.; Zhang, J.; Cheong, W.C.; Yu, R.; Gu, L.; Dong, J.; et al. Carbon nitride supported Fe₂ cluster catalysts with superior performance for alkene epoxidation. *Nat. Commun.* **2018**, *9*, 2353. [\[CrossRef\]](#) [\[PubMed\]](#)
34. Jiang, Y.; Liu, Q.; Tan, K.M.; Wang, F.; Ng, H.Y. Insights into mechanisms, kinetics and pathway of continuous visible-light photodegradation of PPCPs via porous g-C₃N₄ with highly dispersed Fe(III) active sites. *Chem. Eng. J.* **2021**, *423*, 130095. [\[CrossRef\]](#)
35. Wu, X.; Wang, X.; Wang, F.; Yu, H. Soluble g-C₃N₄ nanosheets: Facile synthesis and application in photocatalytic hydrogen evolution. *Appl. Catal. B Environ.* **2019**, *247*, 70–77. [\[CrossRef\]](#)
36. Tonda, S.; Kumar, S.; Kandula, S.; Shanker, V. Fe-doped and mediated graphitic carbon nitride nanosheets for enhanced photocatalytic performance under natural sunlight. *J. Mater. Chem. A* **2014**, *2*, 6772. [\[CrossRef\]](#)
37. Peng, X.; Wu, J.; Zhao, Z.; Wang, X.; Dai, H.; Xu, L.; Xu, G.; Jian, Y.; Hu, F. Activation of peroxymonosulfate by single-atom Fe-g-C₃N₄ catalysts for high efficiency degradation of tetracycline via nonradical pathways: Role of high-valent iron-oxo species and Fe-N_x sites. *Chem. Eng. J.* **2021**, *427*, 130803. [\[CrossRef\]](#)
38. Luo, T.; Hu, X.; She, Z.; Wei, J.; Feng, X.; Chang, F. Synergistic effects of Ag-doped and morphology regulation of graphitic carbon nitride nanosheets for enhanced photocatalytic performance. *J. Mol. Liq.* **2021**, *324*, 114772. [\[CrossRef\]](#)
39. Li, Y.; Lv, K.; Ho, W.; Dong, F.; Wu, X.; Xia, Y. Hybridization of rutile TiO₂ (rTiO₂) with g-C₃N₄ quantum dots (CN QDs): An efficient visible-light-driven Z-scheme hybridized photocatalyst. *Appl. Catal. B Environ.* **2017**, *202*, 611–619. [\[CrossRef\]](#)
40. Chang, F.; Li, C.; Luo, J.; Xie, Y.; Deng, B.; Hu, X. Enhanced visible-light-driven photocatalytic performance of porous graphitic carbon nitride. *Appl. Surf. Sci.* **2015**, *358*, 270–277. [\[CrossRef\]](#)
41. Meng, Y.; Zhang, L.; Jiu, H.; Zhang, Q.; Zhang, H.; Ren, W.; Sun, Y.; Li, D. Construction of g-C₃N₄/ZIF-67 photocatalyst with enhanced photocatalytic CO₂ reduction activity. *Mater. Sci. Semicond. Process.* **2019**, *95*, 35–41. [\[CrossRef\]](#)
42. Xiao, J.; Xie, Y.; Nawaz, F.; Wang, Y.; Du, P.; Cao, H. Dramatic coupling of visible light with ozone on honeycomb-like porous g-C₃N₄ towards superior oxidation of water pollutants. *Appl. Catal. B Environ.* **2016**, *183*, 417–425. [\[CrossRef\]](#)
43. Wang, Y.; Zhao, X.; Cao, D.; Wang, Y.; Zhu, Y. Peroxymonosulfate enhanced visible light photocatalytic degradation bisphenol A by single-atom dispersed Ag mesoporous g-C₃N₄ hybrid. *Appl. Catal. B Environ.* **2017**, *211*, 79–88. [\[CrossRef\]](#)
44. Xiao, X.; Gao, Y.; Zhang, L.; Zhang, J.; Zhang, Q.; Li, Q.; Bao, H.; Zhou, J.; Miao, S.; Chen, N.; et al. A promoted charge separation/transfer system from Cu single atoms and C₃N₄ layers for efficient photocatalysis. *Adv. Mater.* **2020**, *32*, e2003082. [\[CrossRef\]](#)
45. Gan, G.; Li, X.; Wang, L.; Fan, S.; Mu, J.; Wang, P.; Chen, G. Active sites in single-atom Fe-N(x)-C nanosheets for selective electrochemical dechlorination of 1,2-dichloroethane to ethylene. *ACS Nano* **2020**, *14*, 9929–9937. [\[CrossRef\]](#)
46. Wu, Y.; Ding, Y.; Han, X.; Li, B.; Wang, Y.; Dong, S.; Li, Q.; Dou, S.; Sun, J.; Sun, J. Modulating coordination environment of Fe single atoms for high-efficiency all-pH-tolerated H₂O₂ electrochemical production. *Appl. Catal. B Environ.* **2022**, *315*, 121578. [\[CrossRef\]](#)
47. Deng, L.; Qiu, L.; Hu, R.; Yao, L.; Zheng, Z.; Ren, X.; Li, Y.; He, C. Restricted diffusion preparation of fully-exposed Fe single-atom catalyst on carbon nanospheres for efficient oxygen reduction reaction. *Appl. Catal. B Environ.* **2022**, *305*, 121058. [\[CrossRef\]](#)
48. Song, Y.; Zhu, S.; Zhang, S.; Fu, Y.; Wang, L.; Zhao, X.; Yang, B. Investigation from chemical structure to photoluminescent mechanism: A type of carbon dots from the pyrolysis of citric acid and an amine. *J. Mater. Chem. C* **2015**, *3*, 5976–5984. [\[CrossRef\]](#)
49. Hu, J.; Zhang, P.; An, W.; Liu, L.; Liang, Y.; Cui, W. In-situ Fe-doped g-C₃N₄ heterogeneous catalyst via photocatalysis-Fenton reaction with enriched photocatalytic performance for removal of complex wastewater. *Appl. Catal. B Environ.* **2019**, *245*, 130–142. [\[CrossRef\]](#)
50. Zeng, Y.; Liu, X.; Liu, C.; Wang, L.; Xia, Y.; Zhang, S.; Luo, S.; Pei, Y. Scalable one-step production of porous oxygen-doped g-C₃N₄ nanorods with effective electron separation for excellent visible-light photocatalytic activity. *Appl. Catal. B Environ.* **2018**, *224*, 1–9. [\[CrossRef\]](#)
51. Guo, H.; Niu, H.-Y.; Liang, C.; Niu, C.-G.; Liu, Y.; Tang, N.; Yang, Y.; Liu, H.-Y.; Yang, Y.-Y.; Wang, W.-J. Few-layer graphitic carbon nitride nanosheet with controllable functionalization as an effective metal-free activator for peroxymonosulfate photocatalytic activation: Role of the energy band bending. *Chem. Eng. J.* **2020**, *401*, 126072. [\[CrossRef\]](#)
52. Ahmad, I. Comparative study of metal (Al, Mg, Ni, Cu and Ag) doped ZnO/g-C₃N₄ composites: Efficient photocatalysts for the degradation of organic pollutants. *Sep. Purif. Technol.* **2020**, *251*, 117372. [\[CrossRef\]](#)
53. Bian, S.; Li, X.; Zhang, L.; Wang, L.; Wang, J.; Xu, Q.; Zang, L.; Zhang, Y.; Sun, L. Bimetal Cu and Fe modified g-C₃N₄ sheets grown on carbon skeleton for efficient and selective photocatalytic reduction of CO₂ to CO. *J. Environ. Chem. Eng.* **2023**, *11*, 109319. [\[CrossRef\]](#)

54. Chang, F.; Lei, B.; Yang, C.; Wang, J.; Hu, X. Ultra-stable $\text{Bi}_4\text{O}_5\text{Br}_2/\text{Bi}_2\text{S}_3$ n-p heterojunctions induced simultaneous generation of radicals $\cdot\text{OH}$ and $\cdot\text{O}_2^-$ and no conversion to nitrate/nitrite species with high selectivity under visible light. *Chem. Eng. J.* **2021**, *413*, 127443. [\[CrossRef\]](#)
55. Zhu, Z.; Lu, Z.; Wang, D.; Tang, X.; Yan, Y.; Shi, W.; Wang, Y.; Gao, N.; Yao, X.; Dong, H. Construction of high-dispersed $\text{Ag}/\text{Fe}_3\text{O}_4/\text{g-C}_3\text{N}_4$ photocatalyst by selective photo-deposition and improved photocatalytic activity. *Appl. Catal. B Environ.* **2016**, *182*, 115–122. [\[CrossRef\]](#)
56. Yan, S.; Shi, Y.; Tao, Y.; Zhang, H. Enhanced persulfate-mediated photocatalytic oxidation of bisphenol A using bioelectricity and a $\text{g-C}_3\text{N}_4/\text{Fe}_2\text{O}_3$ heterojunction. *Chem. Eng. J.* **2019**, *359*, 933–943. [\[CrossRef\]](#)
57. Xia, P.; Zhu, B.; Cheng, B.; Yu, J.; Xu, J. 2D/2D $\text{g-C}_3\text{N}_4/\text{MnO}_2$ nanocomposite as a direct Z-scheme photocatalyst for enhanced photocatalytic activity. *ACS Sustain. Chem. Eng.* **2017**, *6*, 965–973. [\[CrossRef\]](#)
58. Zhou, Y.; Zhang, C.; Huang, D.; Wang, W.; Zhai, Y.; Liang, Q.; Yang, Y.; Tian, S.; Luo, H.; Qin, D. Structure defined 2D $\text{Mo}_2\text{C}/2\text{D g-C}_3\text{N}_4$ van der Waals heterojunction: Oriented charge flow in-plane and separation within the interface to collectively promote photocatalytic degradation of pharmaceutical and personal care products. *Appl. Catal. B Environ.* **2022**, *301*, 120749. [\[CrossRef\]](#)
59. Zhu, Z.; Ma, C.; Yu, K.; Lu, Z.; Liu, Z.; Yan, Y.; Tang, X.; Huo, P. Fabrication of CoFe_2O_4 -modified and HNTs-supported $\text{g-C}_3\text{N}_4$ heterojunction photocatalysts for enhancing MBT degradation activity under visible light. *J. Mater. Sci.* **2019**, *55*, 4358–4371. [\[CrossRef\]](#)
60. Zhu, Z.; Yu, Y.; Dong, H.; Liu, Z.; Li, C.; Huo, P.; Yan, Y. Intercalation effect of attapulgite in $\text{g-C}_3\text{N}_4$ modified with Fe_3O_4 quantum dots to enhance photocatalytic activity for removing 2-mercaptobenzothiazole under visible light. *ACS Sustain. Chem. Eng.* **2017**, *5*, 10614–10623. [\[CrossRef\]](#)
61. Zhu, Z.; Lu, Z.; Zhao, X.; Yan, Y.; Shi, W.; Wang, D.; Yang, L.; Lin, X.; Hua, Z.; Liu, Y. Surface imprinting of a $\text{g-C}_3\text{N}_4$ photocatalyst for enhanced photocatalytic activity and selectivity towards photodegradation of 2-mercaptobenzothiazole. *RSC Adv.* **2015**, *5*, 40726–40736. [\[CrossRef\]](#)
62. Wu, H.; Wang, D.; Zhou, P.; Xie, M.; Jing, J.; Xu, Y.; Xie, J. Probing effective charge migration and highly improved photocatalytic activity on polyaniline/ $\text{Zn}_3\text{In}_2\text{S}_6$ nano-flower under long wavelength light. *Sep. Purif. Technol.* **2021**, *274*, 119004. [\[CrossRef\]](#)
63. Zhu, Z.; Tang, X.; Wang, T.; Fan, W.; Liu, Z.; Li, C.; Huo, P.; Yan, Y. Insight into the effect of co-doped to the photocatalytic performance and electronic structure of $\text{g-C}_3\text{N}_4$ by first principle. *Appl. Catal. B Environ.* **2019**, *241*, 319–328. [\[CrossRef\]](#)

Disclaimer/Publisher's Note: The statements, opinions and data contained in all publications are solely those of the individual author(s) and contributor(s) and not of MDPI and/or the editor(s). MDPI and/or the editor(s) disclaim responsibility for any injury to people or property resulting from any ideas, methods, instructions or products referred to in the content.